Cation disorder in MgSnN$_2$ and its effects on the electronic properties

Jing Huang[1] and Jun Kang [1,2,*]

[1]*Beijing Computational Science Research Center, 100193 Beijing, China*
[2]*Department of Physics, Beijing Normal University, Beijing 100875, China*

Ternary nitride MgSnN$_2$ is a promising candidate to fill the "green gap" of nitride-based light-emitting diodes. The coexistence of two different valence cations offers a unique tunability on its electronic properties through controlling the degree of cation site ordering without a concomitant change in stoichiometry. In this work, the structural and electronic properties of cation-disordered MgSnN$_2$ are studied through a combination of density functional theory calculations, cluster expansion, and Monte Carlo simulations. The order-disorder phase transition is analyzed, and the short-range and long-range order parameters quantifying the degree of disorder are calculated. A strong correlation between the two parameters is observed, indicating the absence of the octet-rule-conserving disorder. Cation disorder has two main effects on the electronic properties of MgSnN$_2$. One is the reduction of the band gap, and the other is the strong localization of valence band edge states. Further analysis showed that the localization is a consequence of the weak interatomic coupling between the N atoms and the disorder-induced fluctuation of the local electrostatic potentials on the N atoms. These results could be helpful for the understanding of disorder effects in MgSnN$_2$, as well as the tuning of its properties through the control of cation ordering.

I. INTRODUCTION

Recently, heterovalent ternary nitrides, II-IV-N$_2$, have attracted much attention due to their rich ternary chemistry, tunable material properties, and earth abundance of the elemental sources [1–6]. The II-IV-N$_2$ compounds typically have a wurtzite-derived structure with comparable lattice parameters to III-N semiconductors [7–10]. The band gap of the II-IV-N$_2$ compounds covers the visible spectrum and extends into the IR and UV region [11,12]. The coexistence of two different valence cations in II-IV-N$_2$ offers a unique tunability on their electronic properties through controlling the degree of cation site ordering without a concomitant change in stoichiometry [13–18]. Experimentally, the control of cation ordering in II-IV-N$_2$ can be realized by systematically varying growth parameters such as the substrate temperature, II/IV flux ratio, and nitrogen flow rate [7,16,19,20]. Hence, complementary to the well-studied III-N semiconductors, II-IV-N$_2$ compounds have emerged as potential candidates for various optoelectronic applications, such as photovoltaics [21] light-emitting diodes (LEDs) [22], and nonlinear optics [23,24].

A long-standing challenge in nitride-based LEDs is filling the "green gap," impeded by the restricted availability of wurtzite-compatible semiconductors with a band gap of 1.8 to 2.5 eV. MgSnN$_2$, a member of the II-IV-N$_2$ family, has been synthesized recently [8,11,25,26] and exhibits a direct band gap of ∼2.3 eV determined based on the optical absorption spectrum using the Tauc relation [27]. The ideal gap value makes MgSnN$_2$ a promising material to fulfill the

"green gap," and there have been increased research interests focusing on this material. The ground state structure of MgSnN$_2$ is wurtzite-like but with orthorhombic symmetry Pna2$_1$, belonging to the space group number 33 (SG33) [8]. In the SG33 configuration, each N anion is coordinated by two Sn and two Mg cations, satisfying the octet rule, and the arrangement of the Mg and Sn cations is fully ordered. However, both theoretical and experimental studies demonstrated that there could be cation disorder induced by the exchange of Sn and Mg in MgSnN$_2$, which greatly impacts its properties [16,28]. For example, the band gap of MgSnN$_2$ is strongly correlated to the order parameter and significantly reduces with increasing degrees of cation disorder [16]. Hence, the control of cation ordering could be an effective approach to the band gap tuning of MgSnN$_2$, offering good flexibility to fulfill the requirements for various applications. Theoretical calculations revealed that MgSnN$_2$ is prone to partial disorder, but full randomness is difficult to approach. Moreover, the states at the valence band edge become strongly localized in cation-disordered MgSnN$_2$, whereas the conduction band edge is less perturbed [28]. In addition, the unintentional doping in MgSnN$_2$ caused by intrinsic defects is enhanced by cation disorder due to the reduced defect formation energy [29]. Therefore, a comprehensive understanding on the effects of cation disorder in MgSnN$_2$ is crucial to the control of optical and electronic properties of MgSnN$_2$.

Despite the progress already made, there remain many fundamental problems about the cation disorder effects in MgSnN$_2$ that are worth studying. One interesting question is whether the disorder at long-range (several unit cells) and short-range (nearest neighbor) is correlated. According to previous studies, in some II-IV-N$_2$ compounds such as

$ZnSnN_2$, octet-rule-conserving disorder with perfect short-range order (SRO) could occur [30]. In some other II-IV-N_2 compounds like $ZnGeN_2$, such a phase is absent, and the loss in long-range order (LRO) is accompanied by the breaking of octet-rule [31]. Another issue is that the localization of valence band edge states caused by cation disorder is commonly observed in II-IV-N_2 including $MgSnN_2$ [28,32], but the underlying physical mechanism of the localization has not yet explored in detail.

In this work, the structural and electronic properties of cation-disordered $MgSnN_2$ are studied through a combination of density functional theory (DFT) calculations, cluster expansion (CE), and Metropolis Monte Carlo (MC) simulations. The order-disorder phase transition is analyzed, and the SRO and LRO parameters quantifying the degree of disorder are calculated. A linear correlation between SRO and LRO indicates the absence of the octet-rule-conserving disorder. Representative disordered configurations from MC simulations are subsequently relaxed by DFT, and the electronic properties are calculated. The dependence of the band gap and band edge positions on the order parameters is further investigated, and the role of disorder-induced potential fluctuation in creating the localized valence band states is highlighted. These results could be helpful for the understanding of disorder effects in $MgSnN_2$, as well as the tuning of its properties through the control of cation ordering.

II. COMPUTATIONAL MODEL AND METHODS

DFT calculations were performed using the Vienna ab initio Simulation Package (VASP) with plane-wave basis sets [33,34], and the core-valence interaction was described by the projector-augmented wave (PAW) method [35]. The standard PAW pseudopotentials of VASP were used. The valence states include Mg-3s, Sn-4d5s5p, and N-2s2p orbitals. The Perdew-Burke-Ernzerhof (PBE) exchange-correlation functional [36] was adopted for structural relaxation and total energy calculations, with a 400 eV energy cutoff. The thresholds for total energy convergence and structural relaxation are 10^{-5} eV and 10^{-2} eV/Å, respectively. To overcome the band gap underestimation of PBE, the modified Becke-Johnson (mBJ) potential [37,38] was employed to calculate the electronic structure, which is able to yield a reasonable band gap similar to hybrid functionals or GW calculations, and a 500 eV energy cutoff was adopted. Note the mBJ functional is adopted only for the electronic structure calculations because it is a potential-only functional and cannot give Hellmann-Feynman forces. Total energy-related properties are calculated using PBE which predicts overall accurate structural properties and cohesive energies for a diverse type of materials, especially semiconductors [39]. A $5 \times 5 \times 5$ k-point mesh is used for the calculations of the $MgSnN_2$ unit cell, and the Γ point is used for the supercells. Further increasing the mesh size results in a negligible change of results according to our tests.

To explore the effects of cation disorder in $MgSnN_2$, we constructed a CE Hamiltonian using the Alloy Theoretic Automated Toolkit (ATAT) code [40]. As a supercell approach, the CE method explicitly considers local configurations of atomic arrangements. Thus CE is superior in capturing short-range ordering, which could be significant in $MgSnN_2$,

compared to nonstructural approaches for disordered systems such as the coherent potential approximation (CPA), since the latter drops the information about local chemical environments and neglects short-range ordering [41,42]. In the CE approach, the cation disordered $MgSnN_2$ is viewed as a stoichiometric Mg-Sn nitride alloy, and the total energy per cation of a configuration σ of cation occupation can be fitted by the following CE Hamiltonian [41]:

$$E(\sigma) = \sum_{\alpha} J_{\alpha} \overline{\Pi}_{\alpha}(\sigma) \tag{1}$$

Here, the total energy of the fully random cation distribution is taken as the zero reference. α refers to a cluster (pairs, triplets, quadruplets, etc.), and J_{α} is the effective cluster interaction (ECI) for α (including the multiplicity of symmetry-equivalent clusters). $\overline{\Pi}_{\alpha}(\sigma)$ is the average of the atomic correlation functions of the cluster α. The atomic structures in the training set of the CE fitting are based on a $2 \times 2 \times 2$ supercell including 128 atoms which is generated by a 16-atom ideal wurtzite cell with eight generic cation sites. Sixty-six stoichiometric configurations with a 1:1 Mg/Sn ratio but different levels of cation disorder were constructed by switching the Mg and Sn atoms in the fully ordered structure. The total energies of these structures were calculated by DFT with full a relaxation of atomic positions and lattice parameters, and then fitted into Eq. (1). A basis set of clusters consisting of 9 pairs with a maximum distance of 8 Å was considered during the CE fitting.

With the CE Hamiltonian, we performed MC simulations to study the equilibrium cation distribution using a $4 \times 4 \times 4$ supercell including 1024 atoms. It has been shown this supercell is sufficient to achieve size-convergence of MC simulations for II-IV-N_2 materials [31]. We started from a fully randomized cation distribution in $MgSnN_2$. The supercell was first equilibrated at 4000 K and then cooled down to 100 K at a rate of 10^5 MC steps per K. The structure information was collected from 28 independent MC trajectories. Electronic structure calculations were based on a $3 \times 3 \times 3$ supercell with 432 atoms, with the cation distributions generated from other MC simulations using the same CE Hamiltonian. Following the approach of Refs. [32,43], the eigenvalues in different structures were aligned to that of the SG33 ground state by a potential alignment method. Here, the averaged atomic-site electrostatic potential $\bar{V}$ is taken as the common energy reference, which is calculated as $\bar{V} = \Sigma V_i / N$. Here, V_i is the electrostatic potential on atom i and N is the number of atoms in the supercell. We computed the $\bar{V}$ for several supercells with different volumes V_{vol} and found a good linear relationship. Hence, the potential shift of $\bar{V}$ relative to the SG33 structure can be expressed as $\Delta V_{pot} = \beta \Delta V_{vol}$, where ΔV_{vol} is the volume change in percent relative to the SG33 structure. The calculated β is -102 meV. The offset ΔV_{pot} is subtracted to align the VBM/CBM in different structures.

III. RESULTS

The optimized structure of fully ordered ground state of $MgSnN_2$ is shown in Fig. 1(a). Its unit cell contains 16 atoms and has a wurtzite-like structure with a space group of $Pna2_1$ (SG33). The lattice constants a, b, and c are 5.97,
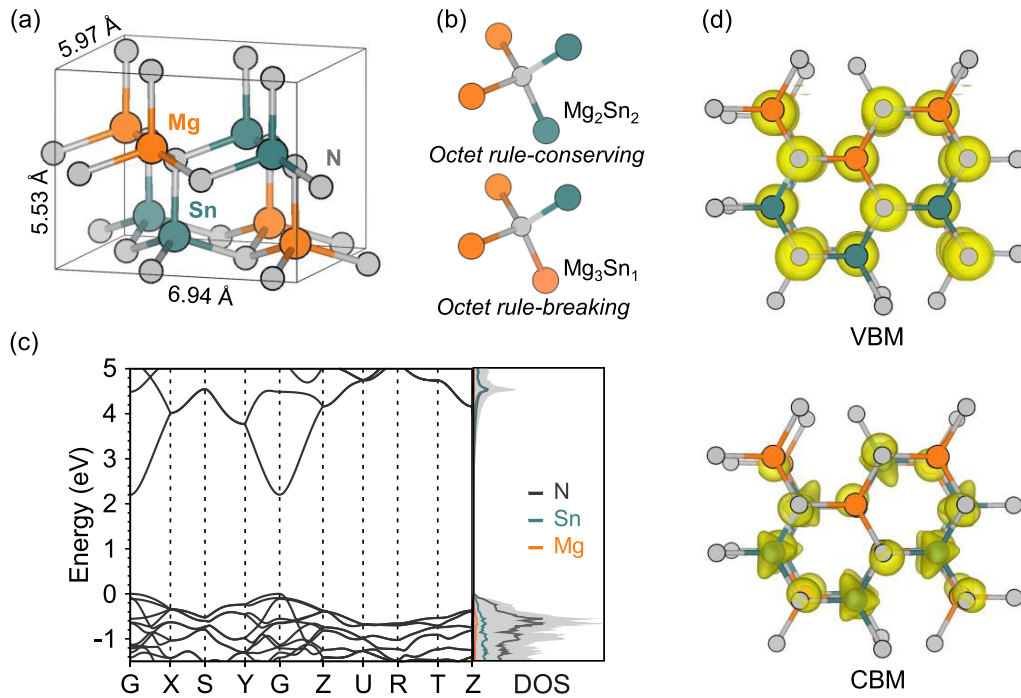
FIG. 1. (a) Optimized unit cell of SG33 MgSnN$_2$. (b) Examples of octet-rule-conserving and octet-rule-breaking tetrahedral motifs. (c) The mBJ calculated band structure and density of states (DOS) of SG33 MgSnN$_2$. (d) The charge densities of VBM (top) and CBM (bottom) at the Gamma point of the Brillouin zone, where the isosurface levels of VBM and CBM are set to 0.004 $e/\text{Å}^3$.

6.94, and 5.53 Å, respectively. The ratio $2a/b$ of 1.720 is slightly smaller than $\sqrt{3}$ in the ideal binary wurtzite and is in good agreement with previous studies [8,44]. In this ordered structure, every N anion is coordinated by two Mg and two Sn cations, such that the N-centered motif (Mg$_2$Sn$_2$) forms a tetrahedron and is locally octet-rule-conserving. Note there is another octet-rule-conserving orthorhombic structure of MgSnN$_2$ with a space group of Pmc2$_1$ (SG26) [8], while its energy is 9.5 meV/cation higher than the SG33 ground structure, according to our calculations. In cation-disordered structures, octet-rule-breaking motifs such as Mg$_3$Sn$_1$ and Mg$_1$Sn$_3$ would appear as Fig. 1(b) shows. The mBJ band structure and density of states (DOS) for SG33 MgSnN$_2$ are shown in Fig. 1(c). It is seen that the band gap is direct. Both the valence band maximum (VBM) and conduction band minimum (CBM) are located at the Gamma point. The mBJ-calculated band gap is 2.20 eV, consistent with previously reported values calculated by hybrid functional (2.22 eV) [28] and GW (2.28 eV) [45]. This value is also in good agreement with the experiment-measured gap of 2.3 eV [27]. The charge densities of the CBM and VBM states are plotted in Fig. 1(d). The VBM is mainly contributed by the N-2p state. Its charge density is strongly concentrated around the N atoms, implying a weak inter-atomic coupling as indicated by the small dispersion and high DOS of the valence band. The CBM is dominated by the s states of Sn and N. The strong interatomic coupling leads to a more delocalized charge density than the VBM. As a result, the conduction band exhibits a large dispersion and a small DOS.

Next, we perform CE fitting to get the ECIs and construct the CE Hamiltonian Eq. (1) of MgSnN$_2$. In Fig. 2(a), the energies predicted by CE against the DFT-calculated energies

are presented, and the deviation is shown in the inset. The error of the fitting is quite small, with a standard deviation of 4.00 meV/cation. The performance of the CE model is further evaluated through the Leave-One-Out Cross Validation approach. In our dataset containing 66 samples, each sample is used once as a test set while the remaining 65 samples form the training set. The process is repeated for every sample in the dataset and the average error is defined as the cross validation (CV) score [46], which estimates the accuracy of the model. The constructed CE model has a small CV score of 4.49 meV/cation. The small CV score indicates that the fitted CE Hamiltonian can well describe the total energy of cation-disordered MgSnN$_2$. The fitted ECIs for the nine pairs are shown in Fig. 2(b). The magnitude of the ECIs decreases as the atom-atom distance in the pair decreases. Moreover, all the ECIs are positive, indicating that the clustering of Mg or Sn is not favored.

Based on the CE Hamiltonian, MC simulations were performed in a temperature window of 100 to 4000 K. Note the thermal scale here should be interpreted as an effective temperature (T_{eff}) which governs the configurational entropy of disorder resulting from nonequilibrium growth, as discussed in previous studies [30,31]. In Fig. 3(a), the dependence of the total energy on the effective temperature is plotted. It is seen that at low temperatures, the system remains at the ground state and the energy is almost independent of the temperature. However, in the region of 1900–2000 K, the energy increases sharply by 70 meV/cation, indicating an order-disorder phase transition. After the transition, the energy increases slowly by 36 meV/cation as the temperature further increases from 2000 to 4000 K. An interesting question is how the calculated transition temperature of 1900 to 2000 K is related to
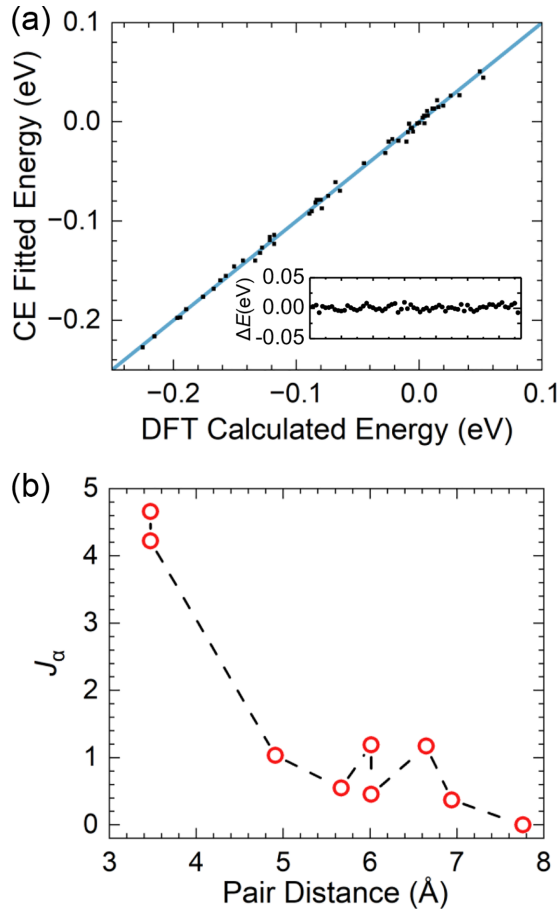
FIG. 2. (a) The DFT calculated and the cluster expansion fitted total energies per cation, where the total energy of the fully random cation distribution is taken as the zero reference. The deviation ΔE between the CE-fitted and DFT-calculated energies is plotted in the inset. (b) Fitted ECIs of pairs from the nearest to the ninth neighbors. Note the the multiplicity of symmetry-equivalent clusters is included.

experiments. As we mentioned, the T_{eff} is a measurement of the degree of cation disorder due to nonequilibrium growth, so it does not exactly correspond to the growth temperature (T_{gr}) in experiments. Experimentally, the disorder-to-order transition of $MgSnN_2$ is observed when the growth temperature increases from ~ 700 K to ~ 900 K [19]. It is obvious that such a transition is not thermodynamic and should be attributed to nonequilibrium effects as the degree of ordering increases with increasing T_{gr}. As discussed in previous studies [30,31], the nonequilibrium effects such as kinetic trapping during low-temperature growth results in more randomness (thus higher T_{eff}) in the cation occupation than what would be anticipated from fully equilibrated thermodynamics. Such effects are gradually reduced with increasing T_{gr} as atomic diffusion allows for the partial equilibration of the cation configuration, so that the difference between T_{eff} and T_{gr} is reduced. As a result, the T_{eff} and T_{gr} could have an inverse relationship at the low-temperature end. [31] In this sense, we may roughly associate the T_{eff} interval of 1900 to 2000 K to the T_{gr} window of 900 to 700 K.

To examine the atomic structure of disordered $MgSnN_2$ in further detail, we calculated the fractions x_{ij} of the

N-centered tetrahedral motifs with different local environments. Here $x_{ij} = n_{ij}/N_N$, where n_{ij} indicates the number of the Mg_iSn_j motifs, and N_N is the number of nitrogen atoms in the supercell. In the SG33 structure, $x_{22} = 1$ and other x_{ij} are 0. As seen in Fig. 3(b), in the window 1900–2000 K, x_{22} rapidly decreases from 1 to 0.66, while x_{31} and x_{13} grow from 0 to 0.17. The partial replacement of the Mg_2Sn_2 motifs by the Mg_3Sn_1 Mg_1Sn_3 motifs is in accordance with the order-disorder transition. Further increasing the temperature only slightly reduces x_{22} and increases x_{31} and x_{13}. In addition, the concentrations of the Mg_4Sn_0 and Mg_0Sn_4 motifs are extremely low, less than 0.01 in the whole temperature range considered. It is noted that even at a T_{eff} of 4000 K, the values of x_{ij} significantly deviate from those in a fully random cation distribution [0.375 for x_{22}, 0.25 for x_{31} and x_{13}, and 0.0625 for x_{40} and x_{04}, as marked in Fig. 3(b)], which suggests the existence of partial SRO. The x_{22} describes the fraction of octet-rule-conserving motifs and one can use it as an SRO parameter $\eta_{\text{SRO}}(x_{22})$ to describe the degree of SRO [31]. Besides x_{22}, which reflects the disorder at nearest neighbors, another relevant quantity to probe the degree of disorder is the LRO parameter η_{LRO}, which is a measurement of the disorder of overall periodicity [47,48]. For $MgSnN_2$, η_{LRO} can be defined as $\eta_{\text{LRO}} = O_{\text{Mg}} + O_{\text{Sn}} - 1$, where O_{Mg} (O_{Sn}) is the fraction of Mg (Sn) sites (referenced to the SG33 structure) occupied by Mg (Sn) atoms in the disordered structure. η_{LRO} is 0 (1) for fully disordered (ordered) structures. In Fig. 3(c), the calculated η_{LRO} as a function of T_{eff} is shown. At low temperatures the η_{LRO} is 1, indicating that the initial random structure evolves into the ordered SG33 ground state after the annealing from 4000 K to 100 K. A sharp drop of η_{LRO} from 1 to 0.1 around the order-disorder transition region is observed. At higher temperatures, η_{LRO} fluctuates around 0.1. The relationship between x_{22} and η_{LRO} is shown in Fig. 3(d), which reveals a linear relationship between them during the order-disorder transition. The observed trend suggests a strong correlation between the SRO and LRO in $MgSnN_2$, namely, the decrease in LRO is accompanied by the breaking of the octet rule in the N-centered motifs. As a result, octet-rule-conserving disorder, which preserves SRO and could exist in the structurally similar $ZnSnN_2$ [30], is less likely to occur in $MgSnN_2$. The different behaviors can be attributed to the more significant contribution of LRO to the total energy of $MgSnN_2$, as indicated by the considerable magnitudes of the ECIs for the pairs beyond the nearest neighbor [see Fig. 2(b)]. This also makes the total energy difference between the octet-rule-conserving SG33 and SG26 structures of $MgSnN_2$ (9.5 meV/cation according to our calculations and 10 meV/cation according to Ref. [8]) several times larger than that of $ZnSnN_2$ (2.2 meV/cation according to our calculations and 1 meV/cation according to Ref. [49]).

The presence of cation disorder in II-IV-N_2 would significantly alter their electronic structures. As the LRO and SRO are strongly correlated in $MgSnN_2$, here we willfocus on the dependence of its electronic structure on the SRO parameter x_{22}. Based on a $3 \times 3 \times 3$ supercell with 432 atoms, we generated structures with different degrees of cation disorder by MC simulations using the CE Hamiltonian, and then performed DFT calculations to explore the electronic properties. Since the concentration of the Mg_4Sn_0 and Mg_0Sn_4 motifs
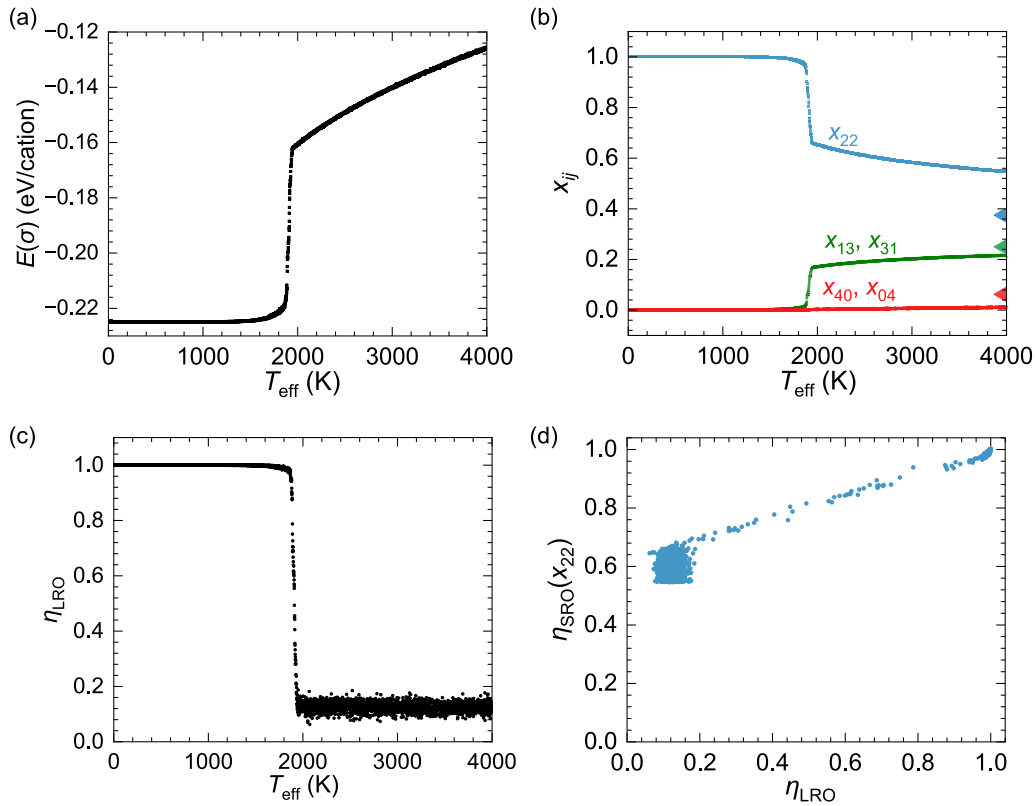
FIG. 3. CE-based MC simulations using a 1024-atom cell. (a) The total energy per cation, (b) the motif fractions x_{ij}, and (c) the LRO parameter η_{LRO} as a function of the effective temperature. The triangles in (b) indicate the motif fractions in a fully random structure for Mg$_2$Sn$_2$, Mg$_3$Sn$_1$ (Mg$_1$Sn$_3$) and Mg$_4$Sn$_0$ (Mg$_0$Sn$_4$) from top to bottom. (d) The relationship between SRO and LRO parameters.

is negligible, here we mainly consider the structures without these two motifs. In Figs. 4(a) and 4(c), the band structures of two structures with slight ($x_{22} = 0.97$) and significant

($x_{22} = 0.58$) disorder are presented. Despite the large difference in x_{22}, the band structures share some common features. Regardless of the degree of disorder, the dispersion of the
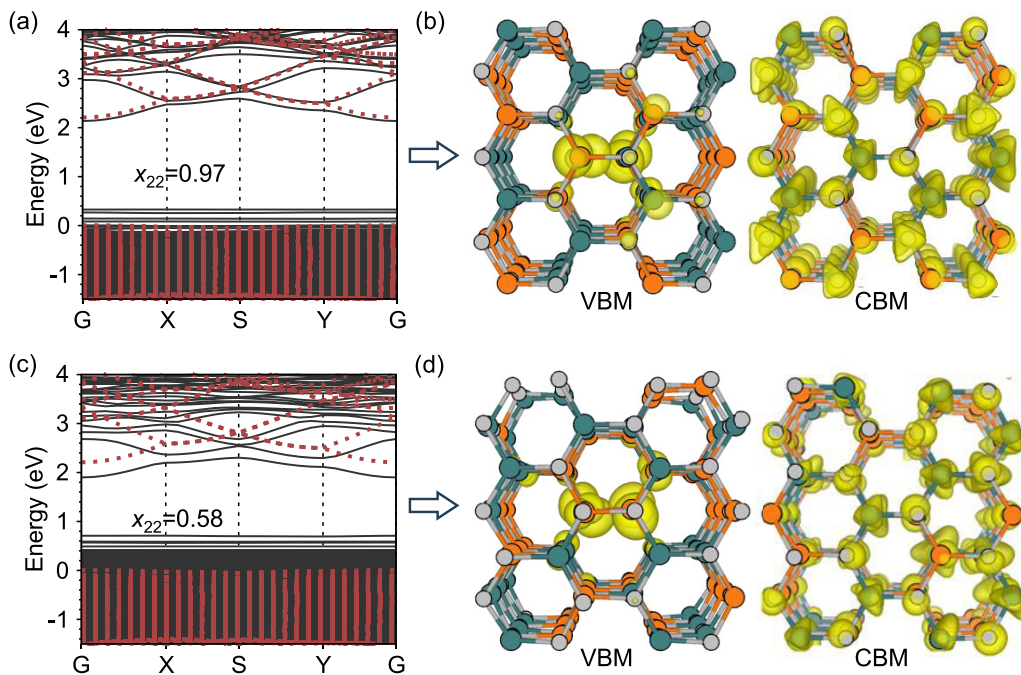

FIG. 4. (a) The band structure for a 432-atom-supercell with $x_{22} = 0.97$. The red dashed lines indicate the band structure of the SG33 MgSnN$_2$ with the same supercell, whose VBM is set to 0. (b) The VBM and CBM charge densities for the structure in (a). The isosurface levels of VBM and CBM are set to 0.004 $e/\text{Å}^3$. (c)-(d) The same as (a)-(b) but for a supercell with $x_{22} = 0.58$.
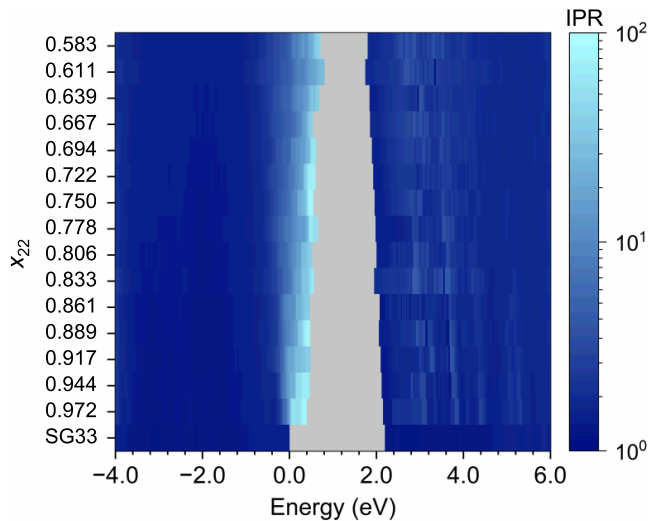
FIG. 5. IPRs of 432-atom $MgSnN_2$ configurations with different x_{22}, including the SG33 ground structure.

FIG. 6. The averaged band edge positions as a function of x_{22}. The VBM positions corresponding to three definitions are presented: unlimited IPR (no cutoff), IPR < 10 (mid-cutoff), IPR < 5 (low-cutoff).

conduction bands in the two structures is similar to that in the fully ordered SG33 structure. However, in both structures with disorder, some isolated and dispersion-less bands appear at the top of the valence bands. In Figs. 4(b) and 4(d), the charge densities of the CBM and VBM states in the two structures are plotted. Unless specified otherwise, here we refer to the lowest unoccupied state as the CBM and the highest occupied state as the VBM. It is seen that the CBM states are quite delocalized and mainly come from the s orbitals of the Sn and N atoms, the same as the case of the ground state structure. In contrast, the VBM states are contributed by the p orbitals of only a few N atoms centered at Mg_3Sn_1 motifs and exhibit strong localization, much like defect states. This occurs even when there is only a slight disorder ($x_{22} = 0.97$). According to our test calculations, the charge density of the localized state given by the HSE functional is almost identical to that from the mBJ functional. Hence, the mBJ can well describe the localization.

The degree of localization of a state at a given energy can be quantified by the inverse participation ratio (IPR) [50]:

$$\mathrm{IPR}(E) = \frac{N\sum_i p_i(E)^2}{\left[\sum_i p_i(E)\right]^2}, \qquad (2)$$

where $p_i(E)$ is the site-projected partial density of states of atom i as a function of energy E, and N is the number of atoms in the supercell, which is 432 here. IPR=1 means all the atoms have equal contribution to the state, corresponding to a complete delocalization. An extreme localization of a state on a single atom leads to an IPR of N. Figure 5 shows the IPR of 16 representative structures obtained from MC simulations with x_{22} ranging from 1 to 0.58. For a given x_{22}, the selected structure has a similar VBM/CBM position as the averaged value at this x_{22} (obtained with seven structures). In the fully ordered SG33 structure with a x_{22} of 1, the IPR at the VBM and CBM is 1.45 and 1.16, respectively. For the disordered structures, the IPRs of the states near the bottom of the conduction band are quite small. In all cases we calculated here, the IPR of CBM does not exceed 2, indicating its delocalized character. This is similar to the case of $ZnSnN_2$ [30].
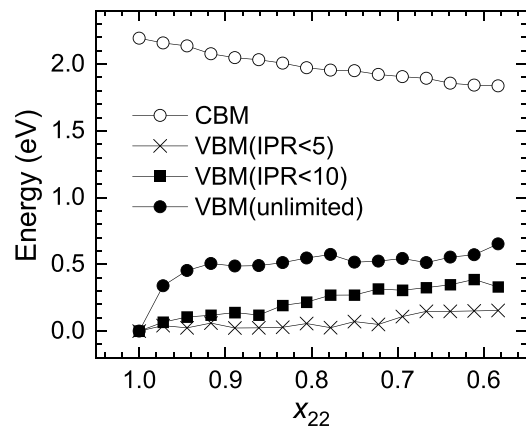
Since the conduction band dispersion in disordered structures is also similar to that of the SG33 structure [Figs. 4(a) and 4(c)], cation disorder is not expected to significantly affect the transport of electrons in $MgSnN_2$. However, the IPRs of the highest valence band states are much larger, ranging from 30 to 80. That is to say, these states are localized typically on only 5 to 15 atoms in the 432-atom supercell, similar to defect states. Therefore, the appearance of octet-rule-breaking disorder is accompanied by strong localization effects around the top of valence bands, creating many defectlike states. In comparison, such disorder causes only moderate localization effects at the valence-band edge of $ZnSnN_2$ [30]. The strong localization could have a significant impact on the hole transport. Instead of band transport in the ordered structure, it is likely that the dominant mechanism of hole transport becomes the hopping between the localized valence states, which usually results in a low carrier mobility [51].

The calculated dependence of the band edge positions on the short-range parameter x_{22} is shown in Fig. 6. At each x_{22}, the results were obtained by averaging over seven configurations in the MC simulation. Due to the strongly localized character of the states at the top of valence bands, there could be different definitions of the VBM in $MgSnN_2$ [32]. The simplest one is taking the highest occupied state as the VBM, as used in the above discussions. However, the top of the valence bands consists of defect-like states, and the band continuum with bulk like and delocalized states is below the highest occupied state. Based on this consideration, one can define an effective VBM as the highest occupied state whose IPR is below a certain threshold, so that it can be viewed as the edge of the band continuum. Following Cordell *et al.* [32], we used criteria of 5 and 10 as mid- and low-IPR cutoff examples. Note the lowest unoccupied state always has an IPR smaller than 2, so the CBM is well defined. It is seen from Fig. 6 that the CBM energy decreases almost linearly by about 0.4 eV when x_{22} reduces from 1 to 0.58. The behaviors of the VBM with different definitions are different. In case the IPR is not limited, the VBM energy increases by 0.5 eV as x_{22} goes from 1 to 0.9, and then stabilizes around 0.5–0.6 eV when the disorder further increases. Consequently,

there is an over 1 eV band gap reduction from 2.20 eV to 1.18 eV from the order structure to $x_{22} = 0.58$. In cases of the mid- and low-IPR cutoff definitions, the VBM energy also increases with reducing x_{22} but with a smaller magnitude, and the relationship is more linearlike. In addition, a smaller IPR criterion leads to a smaller slope. For IPR < 10 and IPR < 5, the VBM increases to ~ 0.35 and ~ 0.15 eV at $x_{22} = 0.58$, and the band gap reduces to 1.51 eV and 1.68 eV, respectively. The contrasting behaviors of the VBM suggest that the sizable band gap reduction in the unlimited IPR definition is largely contributed by the defect-like states in the valence band.

Finally, we'd like to discuss the origin of the strong localization effect in the valence band induced by cation disorder. Because the valence state of Mg is $+2$ whereas that of Sn is $+4$, the presence of cation disorder leads to fluctuation of the local electrostatic potentials on the N sites in MgSnN$_2$. As discussed above, the interatomic coupling in the VBM of the ground state MgSnN$_2$ is weak, thus one can expect that the distribution of the IPR-unlimited VBM in cation disordered MgSnN$_2$ is dominated by the potential fluctuation, and it tends to localize around the N atoms with the highest on-site electrostatic potentials. This is corroborated by the fact that the N atoms contributing significantly to the VBM are always centered at Mg$_3$Sn$_1$ motifs. The Mg ion is less positively charged than the Sn ion, hence the electrostatic potential of an N atom with an Mg-rich environment will be higher. To further demonstrate the effect of potential fluctuation, we plot the relationship between the normalized projected contribution P_i of each N atom to the VBM and VBM $- 1$ states and its on-site electrostatic potential V_i^N in Fig. 7(a). The data are collected from 105 representative structures with different degrees of disorder generated from the MC simulations. For each structure, we selected 30 N atoms with the highest V_i^N, and the V_i^N in different structures are aligned relative to that in the fully ordered structure (i.e., the V_i^N in the SG33 structure is 0). It is notable that the fluctuation of V_i^N is quite large. Even when x_{22} is small (light blue dots), the maximum V_i^N can be over 1.5 eV. Hence the exchange of a single pair of Mg and Sn can induce a large potential shift on the neighboring N sites. When V_i^N is less than 1 eV (which means the energy on the N site is higher than that in the ordered structure by no more than 1 eV), the P_i is quite small. As V_i^N exceeds 1 eV, the P_i increases sharply with increasing V_i^N, demonstrating that the highest occupied states indeed prefer to localize on the N atoms with the highest electrostatic potentials. Besides the spatial distribution, the VBM energy is also dominated by potential fluctuation. In Fig. 7(b), the relationship between the VBM energy in a structure and the maximum V_i^N [V_i^N(max)] in this structure is shown. The results are obtained from 105 structures with different x_{22}. It is clear that there is a linear correlation between the VBM energy and V_i^N(max), and the slope of the linear fitting is 0.96, quite close to 1. It is also noted that a small x_{22} does not necessarily lead to a small V_i^N(max), indicating a short-range nature of the potential fluctuation. As a result, the VBM energy exhibits a weak dependence on x_{22}. The valence band edge localization caused by cation disorder is frequently observed in other II-IV-N$_2$ materials [14,30,32]. Given their similar electronic structures to MgSnN$_2$, we expect the mechanism proposed here to also work for those systems.
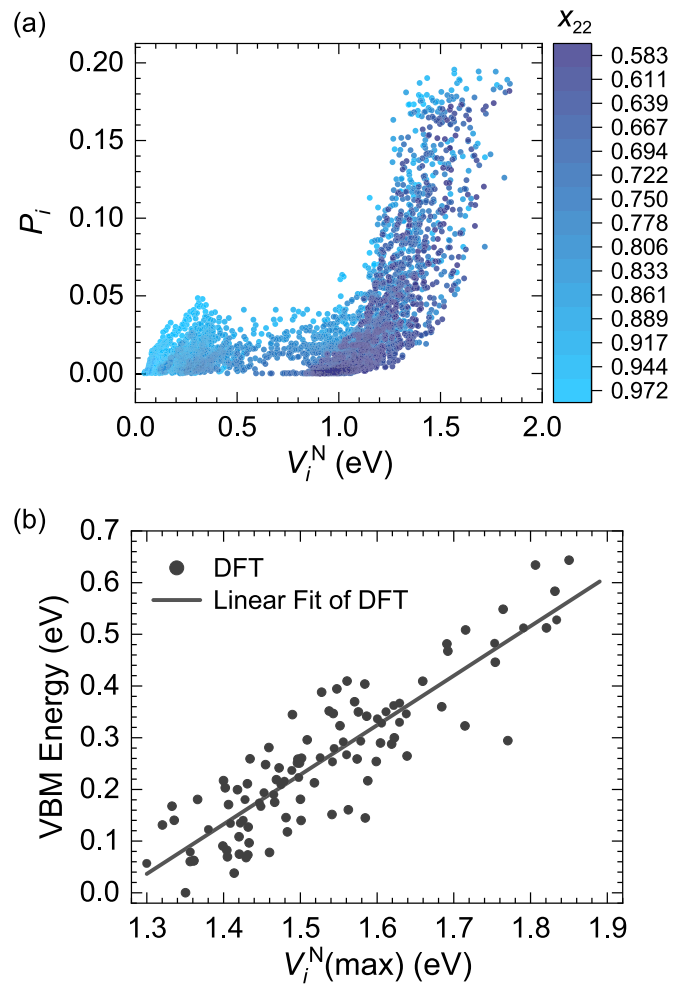

FIG. 7. (a) The relationship between the normalized projected contribution P_i of each N atom to the VBM and VBM $- 1$ states and its on-site electrostatic potential V_i^N. The data are collected from 105 representative structures with different degrees of disorder as indicated by the color bar. For each structure, the 30 highest V_i^N are plotted, and all the V_i^N in different structures are aligned relative to that in the fully ordered structure (set as 0). (b) The relationship between the VBM energy in a structure and the V_i^N(max) in this structure.

IV. CONCLUSION

In summary, by combining DFT calculations, cluster expansion, and MC simulations, the structural and electronic properties of cation-disordered MgSnN$_2$ are investigated. It is found that an order-disorder transition occurs at an effective temperature around 1900 to2000 K. The transition is mainly caused by the partial replacement of the octet-rule-conserving Mg$_2$Sn$_2$ motifs by the octet-rule-breaking Mg$_1$Sn$_3$ and Mg$_3$Sn$_1$ motifs, and the concentrations of the Mg$_4$Sn$_0$ and Mg$_0$Sn$_4$ motifs are extremely low in the temperature range considered. The motif fractions deviate significantly from the case of complete randomness, hence there remains a certain degree of SRO above the transition. Moreover, the SRO and LRO parameters are found to be strongly correlated, indicating the decrease in LRO is accompanied by the loss of SRO.

Thus octet-rule-conserving disorder is not likely to occur in $MgSnN_2$.

Cation disorder has two main effects on the electronic properties $MgSnN_2$. One is the reduction of the band gap which is in accordance with experimental observations. Both the lowering of the CBM and the raising of the VBM contribute to the gap reduction. The other effect of disorder is the defect-like states at the top of the valence band, which strongly localizes at the N atoms with Mg-rich coordination. The localization appears even when there is only a slight disorder. As a result, hopping transport would dominate hole transport in disordered $MgSnN_2$ instead of band transport, resulting in a low carrier mobility. In contrast, the conduction band states remain delocalized and electron transport is less affected by disorder. Further analysis showed that the localization of the valence band states is a consequence of the weak interatomic coupling between the N atoms and the disorder-induced fluctuation of the local electrostatic potentials on the N atoms. We expect this mechanism also works for other II-IV-N_2 materials where valence band edge localization caused by cation disorder is frequently observed.

ACKNOWLEDGMENTS

[1] A. D. Martinez, A. N. Fioretti, E. S. Toberer, and A. C. Tamboli, Synthesis, structure, and optoelectronic properties of II–IV–V_2 materials, J. Mater. Chem. A **5**, 11418 (2017).

[2] I. S. Khan, K. N. Heinselman, and A. Zakutayev, Review of $ZnSnN_2$ semiconductor material, J. Phys. Energy **2**, 032007 (2020).

[3] S. Chen, P. Narang, H. A. Atwater, and L.-W. Wang, Phase stability and defect physics of a ternary $ZnSnN_2$ semiconductor: First principles insights, Adv. Mater. **26**, 311 (2014).

[4] N. Feldberg, J. D. Aldous, W. M. Linhart, L. J. Phillips, K. Durose, P. A. Stampe, R. J. Kennedy, D. O. Scanlon, G. Vardar, R. L. Field, T. Y. Jen, R. S. Goldman, T. D. Veal, and S. M. Durbin, Growth, disorder, and physical properties of $ZnSnN_2$, Appl. Phys. Lett. **103**, 042109 (2013).

[5] A. L. Greenaway, C. L. Melamed, M. B. Tellekamp, R. Woods-Robinson, E. S. Toberer, J. R. Neilson, and A. C. Tamboli, Ternary nitride materials: Fundamentals and emerging device applications, Annu. Rev. Mater. Res. **51**, 591 (2021).

[6] F. Kawamura, H. Murata, M. Imura, N. Yamada, and T. Taniguchi, Synthesis of $CaSnN_2$ via a high-pressure metathesis reaction and the properties of II-Sn-N_2 (II = Ca, Mg, Zn) semiconductors, Inorg. Chem. **60**, 1773 (2021).

[7] E. W. Blanton, K. He, J. Shan, and K. Kash, Characterization and control of $ZnGeN_2$ cation lattice ordering, J. Cryst. Growth **461**, 38 (2017).

[8] A. L. Greenaway, A. L. Loutris, K. N. Heinselman, C. L. Melamed, R. R. Schnepf, M. B. Tellekamp, R. Woods-Robinson, R. Sherbondy, D. Bardgett, S. Bauers, A. Zakutayev, S. T. Christensen, S. Lany, and A. C. Tamboli, Combinatorial synthesis of magnesium tin nitride semiconductors, J. Am. Chem. Soc. **142**, 8421 (2020).

[9] P. C. Quayle, E. W. Blanton, A. Punya, G. T. Junno, K. He, L. Han, H. Zhao, J. Shan, W. R. L. Lambrecht, and K. Kash, Charge-neutral disorder and polytypes in heterovalent wurtzite-based ternary semiconductors: The importance of the octet rule, Phys. Rev. B **91**, 205207 (2015).

[10] N. L. Adamski, D. Wickramaratne, and C. G. Van de Walle, Band alignments and polarization properties of the Zn-IV-nitrides, J. Mater. Chem. C **8**, 7890 (2020).

[11] N. Yamada, M. Mizutani, K. Matsuura, M. Imura, H. Murata, J. Jia, and F. Kawamura, Band gap-tunable (Mg, Zn)SnN_2 earth-abundant alloys with a wurtzite structure, ACS Appl. Electron. Mater. **3**, 4934 (2021).

[12] S. Lyu, D. Skachkov, K. Kash, E. W. Blanton, and W. R. L. Lambrecht, Band gaps, band-offsets, disorder, stability region, and point defects in II-IV-N_2 semiconductors, Physica Status Solidi (a) **216**, 1800875 (2019).

[13] R. R. Schnepf, J. J. Cordell, M. B. Tellekamp, C. L. Melamed, A. L. Greenaway, A. Mis, G. L. Brennecka, S. Christensen, G. J. Tucker, E. S. Toberer, S. Lany, and A. C. Tamboli, Utilizing site disorder in the development of new energy-relevant semiconductors, ACS Energy Lett. **5**, 2027 (2020).

[14] D. Skachkov, P. C. Quayle, K. Kash, and W. R. L. Lambrecht, Disorder effects on the band structure of $ZnGeN_2$: Role of exchange defects, Phys. Rev. B **94**, 205201 (2016).

[15] A. N. Fioretti, A. Zakutayev, H. Moutinho, C. Melamed, J. D. Perkins, A. G. Norman, M. Al-Jassim, E. S. Toberer, and A. C. Tamboli, Combinatorial insights into doping control and transport properties of zinc tin nitride, J. Mater. Chem. C **3**, 11017 (2015).

[16] R. A. Makin, K. York, S. M. Durbin, N. Senabulya, J. Mathis, R. Clarke, N. Feldberg, P. Miska, C. M. Jones, Z. Deng, L. Williams, E. Kioupakis, and R. J. Reeves, Alloy-free band gap tuning across the visible spectrum, Phys. Rev. Lett. **122**, 256403 (2019).

[17] M. Kute, Z. Deng, S. Chae, and E. Kioupakis, Cation-size mismatch as a predictive descriptor for structural distortion, configurational disorder, and valence-band splitting in II-IV-N_2 semiconductors, Appl. Phys. Lett. **119**, 132104 (2021).

[18] S. Ke, J. S. Mangum, A. Zakutayev, A. L. Greenaway, and J. B. Neaton, First-principles studies of the electronic and optical properties of zinc titanium nitride: The role of cation disorder, Chem. Mater. **36**, 3164 (2024).

[19] K. R. York, R. A. Makin, N. Senabulya, J. P. Mathis, R. Clarke, R. J. Reeves, and S. M. Durbin, Growth parameter based control of cation disorder in $MgSnN_2$ thin films, J. Electron. Mater. **50**, 2949 (2021).

[20] R. A. Makin, N. Senabulya, J. Mathis, N. Feldberg, P. Miska, R. Clarke, and S. M. Durbin, Growth of ordered and disordered $ZnSnN_2$, J. Vac. Sci. Technol. B **35**, 02B116 (2017).

[21] A. Laidouci, A. Aissat, and J. Vilcot, Numerical study of solar cells based on $ZnSnN_2$ structure, Solar Energy **211**, 237 (2020).

[22] L. Han, K. Kash, and H. Zhao, Designs of blue and green light-emitting diodes based on type-II InGaN-ZnGeN$_2$ quantum wells, J. Appl. Phys. **120**, 103102 (2016).

[23] G. He, I. Rozahun, Z. Li, J. Zhang, and M.-H. Lee, Size effect and identified superior functional units enhancing second harmonic generation responses on the II-IV-V$_2$ type nonlinear optical crystals, Chem. Phys. **518**, 101 (2019).

[24] T. R. Paudel and W. R. L. Lambrecht, First-principles calculations of elasticity, polarization-related properties, and nonlinear optical coefficients in Zn-IV-N$_2$ compounds, Phys. Rev. B **79**, 245205 (2009).

[25] N. Yamada, K. Matsuura, M. Imura, H. Murata, and F. Kawamura, Composition-dependent properties of wurtzite-type Mg$_{1+x}$Sn$_{1-x}$N$_2$ epitaxially grown on GaN(001) templates, ACS Appl. Electron. Mater. **3**, 1341 (2021).

[26] F. Alnjiman, A. Virfeu, D. Pilloud, S. Diliberto, E. Haye, A. E. Giba, S. Migot, J. Ghanbaja, P. Boulet, H. Albrithen, and J.-F. Pierson, Theoretical and experimental approaches for the determination of functional properties of MgSnN$_2$ thin films, Sol. Energy Mater. Sol. Cells **244**, 111797 (2022).

[27] F. Kawamura, M. Imura, H. Murata, N. Yamada, and T. Taniguchi, Synthesis of a novel rocksalt-type ternary nitride semiconductor MgSnN$_2$ using the metathesis reaction under high pressure, Eur. J. Inorg. Chem. **2020**, 446 (2020).

[28] D. Han, S. S. Rudel, W. Schnick, and H. Ebert, Self-doping behavior and cation disorder in MgSnN$_2$, Phys. Rev. B **105**, 125202 (2022).

[29] F. Ning, J. Huang, and J. Kang, Cation-disorder-enhanced unintentional doping in MgSnN$_2$, Phys. Rev. Appl. **19**, 054046 (2023).

[30] S. Lany, A. N. Fioretti, P. P. Zawadzki, L. T. Schelhas, E. S. Toberer, A. Zakutayev, and A. C. Tamboli, Monte Carlo simulations of disorder in ZnSnN$_2$ and the effects on the electronic structure, Phys. Rev. Mater. **1**, 035401 (2017).

[31] J. J. Cordell, J. Pan, A. C. Tamboli, G. J. Tucker, and S. Lany, Probing configurational disorder in ZnGeN$_2$ using cluster-based Monte Carlo, Phys. Rev. Mater. **5**, 024604 (2021).

[32] J. J. Cordell, G. J. Tucker, A. Tamboli, and S. Lany, Bandgap analysis and carrier localization in cation-disordered ZnGeN$_2$, APL Mater. **10**, 011112 (2022).

[33] G. Kresse and J. Hafner, *Ab initio* molecular dynamics for liquid metals, Phys. Rev. B **47**, 558 (1993).

[34] G. Kresse and J. Furthmüller, Efficient iterative schemes for ab initio total-energy calculations using a plane-wave basis set, Phys. Rev. B **54**, 11169 (1996).

[35] G. Kresse and D. Joubert, From ultrasoft pseudopotentials to the projector augmented-wave method, Phys. Rev. B **59**, 1758 (1999).

[36] J. P. Perdew, K. Burke, and M. Ernzerhof, Generalized gradient approximation made simple, Phys. Rev. Lett. **77**, 3865 (1996).

[37] A. D. Becke and E. R. Johnson, A simple effective potential for exchange, J. Chem. Phys. **124**, 221101 (2006).

[38] F. Tran and P. Blaha, Accurate band gaps of semiconductors and insulators with a semilocal exchange-correlation potential, Phys. Rev. Lett. **102**, 226401 (2009).

[39] G.-X. Zhang, A. M. Reilly, A. Tkatchenko, and M. Scheffler, Performance of various density-functional approximations for cohesive properties of 64 bulk solids, New J. Phys. **20**, 063020 (2018).

[40] A. van de Walle, M. Asta, and G. Ceder, The alloy theoretic automated toolkit: A user guide, Calphad **26**, 539 (2002).

[41] S.-H. Wei, L. G. Ferreira, J. E. Bernard, and A. Zunger, Electronic properties of random alloys: Special quasirandom structures, Phys. Rev. B **42**, 9622 (1990).

[42] M. Karabin, W. R. Mondal, A. Östlin, W.-G. D. Ho, V. Dobrosavljevic, K.-M. Tam, H. Terletska, L. Chioncel, Y. Wang, and M. Eisenbach, *Ab initio* approaches to high-entropy alloys: A comparison of cpa, sqs, and supercell methods, J. Mater. Sci. **57**, 10677 (2022).

[43] S. Lany and A. Zunger, Accurate prediction of defect properties in density functional supercell calculations, Modell. Simul. Mater. Sci. Eng. **17**, 084002 (2009).

[44] B. Dumre, D. Gall, and S. Khare, Stability, and electronic and optical properties of ternary nitride phases of MgSnN$_2$: A first-principles study, J. Phys. Chem. Solids **153**, 110011 (2021).

[45] S. Lyu and W. R. Lambrecht, Quasiparticle self-consistent *GW* band structures of Mg-IV-N$_2$ compounds: The role of semicore d states, Solid State Commun. **299**, 113664 (2019).

[46] A. van de Walle and G. Ceder, Automating first-principles phase diagram calculations, J. Phase Equilib. **23**, 348 (2002).

[47] W. L. Bragg and E. J. Williams, The effect of thermal agitation on atomic arrangement in alloys, Proc. R. Soc. London, Ser. A **145**, 699 (1934).

[48] W. L. Bragg and E. J. Williams, The effect of thermal agitaion on atomic arrangement in alloys-II, Proc. R. Soc. London, Ser. A **151**, 540 (1935).

[49] J. Pan, J. Cordell, G. J. Tucker, A. C. Tamboli, A. Zakutayev, and S. Lany, Interplay between composition, electronic structure, disorder, and doping due to dual sublattice mixing in nonequilibrium synthesis of ZnSnN$_2$:O, Adv. Mater. **31**, 1807406 (2019).

[50] D. Thouless, Electrons in disordered systems and the theory of localization, Phys. Rep. **13**, 93 (1974).

[51] J. Kang, Phonon-assisted hopping through defect states in MoS$_2$: A multiscale simulation, J. Phys. Chem. Lett. **11**, 3615 (2020).